

Conductivity scaling and absence of localization in disordered nodal line semimetals

Carolina Paiva¹ and Jan Behrends²

¹*Raymond and Beverly Sackler School of Physics and Astronomy, Tel Aviv University, Tel Aviv 6997801, Israel*

²*T.C.M. Group, Cavendish Laboratory, University of Cambridge, J.J. Thomson Avenue, Cambridge, CB3 0HE, UK*

Transport plays a key role in characterizing topological insulators and semimetals. Understanding the effect of disorder is crucial to assess the robustness of experimental signatures for topology. In this work, we find the absence of localization in nodal line semimetals for long-range scalar disorder and a large range of disorder strengths. Using a continuum transfer matrix approach, we find that the conductivity in the plane and out of the plane of the nodal line increases with system size and disorder strength. We substantiate these findings by a perturbative calculation and show that the conductivity increases with disorder strength using the Kubo formula in the self-consistent Born approximation. We also find that the system remains metallic for vector disorder and that vector disorder can drive a transition from an insulating to a metallic regime. Our results demonstrate the absence of localization in a bulk system.

I. INTRODUCTION

The scaling theory of localization [1] postulates that the conductance of a disordered electron system at zero temperature scales universally with system size. In a large class of systems of linear dimension L , the logarithmic derivative $\beta(g) = d\log(g)/d\log(L)$, with the dimensionless conductance $g = G/(e^2/h)$ and conductance G , depends only the dimension d and on g itself. Quantum corrections play an important role in two dimensions (2D) [2]: While $\beta \approx 0$ for large g , the sign of $\beta(g \gg 1)$ is determined by the system's symmetry class [3], resulting in a metal-insulator transition, localization at any disorder strength, or critical behavior [2, 4].

Topological systems might defy this expectation. A θ -term [5] drives 2D Dirac fermions into a metallic phase [6] such that they evade localization for all disorder strengths [7, 8]. Similarly, 3D Weyl nodes exhibit a phase transition or crossover [9, 10] from a pseudo-ballistic to a diffusive regime [11] with a positive β function for all disorder strengths [12, 13], providing an example of a non-Anderson disorder-driven phase transition [13, 14].

In this work, we numerically demonstrate that 3D nodal line semimetals subject to long-range disorder remain metallic, even for strong disorder. Nodal line semimetals are topological semimetals where the bands touch in lines in the Brillouin zone [15–17]. Different from Weyl nodes, additional symmetries are necessary to protect this gap closing [16–19]. Following theoretical proposals [20–25], nodal lines close to the Fermi energy have been realized in solid state systems [26–31], photonic crystals [32], and cold atom systems [33].

Long-range disorder in nodal line semimetals may increase the conductivity due to weak anti-localization [34–36]. This is in stark contrast to short-range disorder that results in weak localization [35], and, via a transition from a semimetallic to a metallic regime, eventually to Anderson localization [37]. Weak anti-localization arises when the relevant scattering processes are effectively 2D, whereas the weak localization correction is a 3D effect [35]. Similarly to long-range disorder, a con-

stant line broadening of the Green's function has been found to increase the conductivity [38]. Recent magnetotransport experiments are consistent with weak anti-localization [39–41].

While the weak anti-localization correction is an inherently perturbative result, the behavior beyond the perturbative regime remains elusive. Here we use a nonperturbative transfer matrix approach [7, 42–46] to demonstrate the absence of localization for a nodal ring at zero energy in the presence of long-range scalar disorder, i.e., a smooth disorder potential with exponential correlations. One advantage of the transfer matrix approach is the direct accessibility of the nodal point, which evades subtleties arising from different orders of limits in perturbative calculations. We find that the conductivity increases with disorder and see no indication of localization for strong disorder. For nodal lines whose diameter is larger than the inverse scattering length, we find that the conductivity collapses onto the same line, consistent with the 2D-dominated weak anti-localization regime [35].

We focus on transport out of the plane of the nodal line and complement our results by a perturbative approach in the self-consistent Born approximation (SCBA), which also predicts an unbounded growth of the conductivity with disorder. Furthermore, we show that these conclusions remain true for symmetry-breaking disorder, which can drive the system to a metallic phase, even when starting from a gapped insulator phase. For in-plane transport, we find that the conductivity oscillates with system size in the clean case, and that these oscillations remain visible upon the inclusion of disorder; for clean systems, the conductivity in the limit of large systems does not equal the Kubo formula result, different from out-of-plane transport.

The Fermi surface we consider, i.e., a 1D nodal line embedded in a 3D system, has codimension 2 [18], which, together with the linear dispersion, has led to interpretations of nodal line semimetals as a 3D analog of graphene [26]. The growth of the conductivity with disorder is analogous to the conductivity growth in graphene without intervalley scattering, albeit with one important difference: The unbound growth of the conductivity can

be found only for isolated Dirac nodes [7] as intervalley scattering will eventually lead to localization—the true absence of localization is thus only possible when isolated Dirac nodes arise as surface states of topological insulators [8]. However, isolated nodal lines, as considered in this work, exist in the bulk of lattice systems, and hence the absence of localization does not rely on the absence of certain scattering processes, apart from coupling between bulk and surface states.

This work is organized as follows: We introduce the model for the nodal line semimetal and summarize the transfer matrix method in Sec. II, where we also analytically derive the conductivity for the clean case. In Sec. III, we introduce correlated scalar disorder and present the numerically computed conductivity out of the plane of the nodal line. After comparing these findings with a perturbative approach in Sec. III A, we demonstrate that the metallic regime remains stable for symmetry-breaking disorder in Sec. III B. We briefly discuss in-plane transport in Sec. IV before concluding and discussing potential implications in Sec. V.

II. MODEL AND TRANSPORT IN CLEAN SYSTEMS

We utilize transfer and scattering matrices to compute the conductance of a disordered nodal line semimetal. To this end, we consider a circular nodal line at the chemical potential $\mu = 0$, described by the continuum Hamiltonian [17]

$$\mathcal{H} = \hbar v \sum_{j=1}^3 (k_j \Gamma_j + b_j \Gamma_{j,5}) + m \Gamma_4 + V(\mathbf{r}) \quad (1)$$

where \mathcal{P} denotes path ordering and $u_{\mathbf{q}\perp}(z)$ is the Fourier transform of $u(\mathbf{r})$ along the x and y directions. The transfer matrix T is alternatively described by a corresponding scattering matrix $S = \begin{pmatrix} r & t' \\ t & r' \end{pmatrix}$ with transmission matrices t, t' and reflection matrices r, r' [44, 46]. The dimensionless conductance $g = \text{tr}[t^\dagger t]$ can directly be computed from the transmission matrix.

We pause here to note that we generally need to resort to numerical evaluations of Eq. (4) for disordered systems, as described in detail in Sec. III. In the clean case, however, since the transfer matrix is diagonal in momentum space, the path-ordered exponential equals the matrix exponential. We can find analytical solutions for transport parallel to \mathbf{b} , i.e., $\mathbf{b} = b\mathbf{e}_z$. For simplicity,

with velocity v and momentum \mathbf{k} . Here we consider a scalar disorder potential $V(\mathbf{r}) = u(\mathbf{r})\mathbf{1}$ with the identity matrix $\mathbf{1}$ (we discuss a different type of disorder with a vector potential in Sec. III B). The matrices $\Gamma_{1\dots 4}$ are the Euclidean gamma matrices, i.e., 4×4 Hermitian anticommuting matrices satisfying $\{\Gamma_i, \Gamma_j\} = 2\delta_{ij}$. Their product $\Gamma_5 = \Gamma_1\Gamma_2\Gamma_3\Gamma_4$ is also Hermitian, and we define $\Gamma_{i,j} = (i/2)[\Gamma_i, \Gamma_j]$ with $i < j$ for convenience. In the clean case ($u(\mathbf{r}) = 0$), the Hamiltonian describes the low-energy degrees of freedom of a nodal line semimetal when $\hbar v|\mathbf{b}| > m$: the spectrum is then gapless with a circular nodal line with radius $\sqrt{|\mathbf{b}|^2 - (m/(\hbar v))^2}$ in the plane orthogonal to the vector \mathbf{b} ; when $\hbar v|\mathbf{b}| < m$, a gap opens in the spectrum [17].

To calculate the conductance at the nodal line along the z direction, we switch to real space along z and seek for zero-energy solution of the Hamiltonian ($\mathcal{H}\psi = 0$), given by

$$\frac{d\psi}{dz} = -i\Gamma_3 \left(\sum_{j=1}^2 k_j \Gamma_j + \sum_{j=1}^3 b_j \Gamma_{j,5} + \frac{m}{\hbar v} \Gamma_4 + \frac{u(\mathbf{r})}{\hbar v} \right) \psi. \quad (2)$$

This equation can be formally solved by

$$\psi_{\mathbf{k}\perp}(z) = T_{\mathbf{k}\perp, \mathbf{k}'\perp}(z, z') \psi_{\mathbf{k}'\perp}(z') \quad (3)$$

with the transfer matrix

$$T_{\mathbf{k}\perp, \mathbf{k}'\perp}(z, z') = \mathcal{P} \exp \left\{ -i\Gamma_3 \int_{z'}^z dz'' \left[\left(k_x \Gamma_1 + k_y \Gamma_2 + \frac{m}{\hbar v} \Gamma_4 + \sum_j b_j \Gamma_{j,5} \right) \delta_{\mathbf{k}\perp, \mathbf{k}'\perp} + \frac{u_{\mathbf{k}\perp - \mathbf{k}'\perp}(z'') \mathbf{1}}{\hbar v} \right] \right\} \quad (4)$$

we focus on $m = 0$, and discuss the solution for $m \neq 0$ in Appendix A. When $m = 0$, the system is effectively time-reversal symmetric; we find [47] $\mathcal{H} = \Gamma_2 \mathcal{H}^* \Gamma_2$ for complex Γ_2 and real Γ_1 and Γ_3 .

When choosing $\Gamma_3 = \tau_3 \otimes \sigma_0$, the diagonal 2×2 blocks of $T(k_x, k_y)$ correspond to $[t^\dagger]^{-1}$ and t'^{-1} [44]. The transmission matrix for a system of length $L_z = L$ along the transport direction and width $L_x = L_y = W$ is then

$$t = \begin{pmatrix} \frac{2 \cosh(bL) \cosh(kL)}{\cosh(2bL) + \cosh(2kL)} & \frac{2e^{-i\phi} \sinh(bL) \sinh(kL)}{\cosh(2bL) + \cosh(2kL)} \\ \frac{2e^{i\phi} \sinh(bL) \sinh(kL)}{\cosh(2bL) + \cosh(2kL)} & \frac{2 \cosh(bL) \cosh(kL)}{\cosh(2bL) + \cosh(2kL)} \end{pmatrix}, \quad (5)$$

with momenta $k_x = 2\pi n_x/W$, $k_y = 2\pi n_y/W$ and polar coordinates $k_x = k \cos(\phi)$, $k_y = k \sin(\phi)$. In the limit

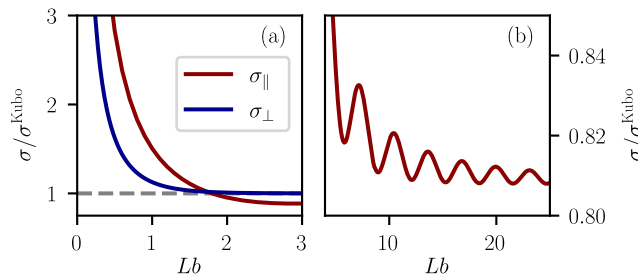


FIG. 1. Conductivity in the clean case for transport out of the plane (σ_{\perp} , blue) and in the plane of the nodal line (σ_{\parallel} , dark red), divided by the Kubo formula result $\sigma_{\perp}^{\text{Kubo}} = b/\pi$ and $\sigma_{\parallel}^{\text{Kubo}} = b/(2\pi)$. Panel (a) shows the exponential decay for short Lb , and panel (b) the oscillations of σ_{\parallel} for large Lb .

$W \gg L$, the dimensionless conductance

$$g_{\perp} = \frac{W^2}{2\pi} \int dk k \text{tr}[t^{\dagger}t] = \frac{W^2 \log[4 \cosh^2(bL)]}{2\pi L^2}. \quad (6)$$

We will henceforth focus on the conductivity $\sigma_{\perp} = g_{\perp}L/W^2$, which we plot for the clean case in Fig. 1. For large systems with $L \gg 1/b$, we recover the Kubo formula result $\sigma_{\perp}^{\text{Kubo}} = b/\pi$ [17], which we will revisit in Sec. III A.

Thus far we have explored the out-of-plane transport in the clean limit. To investigate transport in the plane of the nodal line, we change $\mathbf{b} \rightarrow b\mathbf{e}_x$, and compute the transmission matrix t analog as above, again for $W \gg L$, giving the dimensionless conductance [48]

$$g_{\parallel} = \frac{W^2}{\pi^2} \int \frac{d^2k}{1 + \cos q_+ \cos q_- + \frac{L^2(b^2+k^2)}{q_+q_-} \sin q_+ \sin q_-} \quad (7)$$

with $q_{\pm} = L\sqrt{b^2 - k^2 \pm 2ibk \cos \phi}$. Since we cannot find an analytical solution of this integral, we integrate (7) numerically and show the resulting conductivity $\sigma_{\parallel} = g_{\parallel}L/W^2$ in Fig. 1. Two features are noteworthy: The conductivity oscillates with L with period π/b , Fig. 1(b). The oscillations vanish for large $Lb \gg 1$ (the decay is well-approximated by $\sim 1/(Lb)^{3/2}$ [49]), such that σ_{\parallel} approaches a constant for large systems $L \gg 1/b$. Remarkably, this constant does not equal the Kubo formula result $\sigma_{\parallel}^{\text{Kubo}} = b/(2\pi)$, but approximately $\sigma_{\parallel}/\sigma_{\parallel}^{\text{Kubo}} \approx 0.81$.

III. OUT-OF-PLANE TRANSPORT IN DISORDERED SYSTEMS

We now turn to disordered systems. To this end, we consider long-range disorder with $\langle u(\mathbf{r}) \rangle_{\text{dis}} = 0$ and correlations

$$\langle u(\mathbf{r})u(\mathbf{r}') \rangle_{\text{dis}} = \frac{K_0}{(2\pi)^{3/2}} \left(\frac{\hbar v}{\xi} \right)^2 \exp\left(-\frac{(\mathbf{r} - \mathbf{r}')^2}{2\xi^2}\right) \quad (8)$$

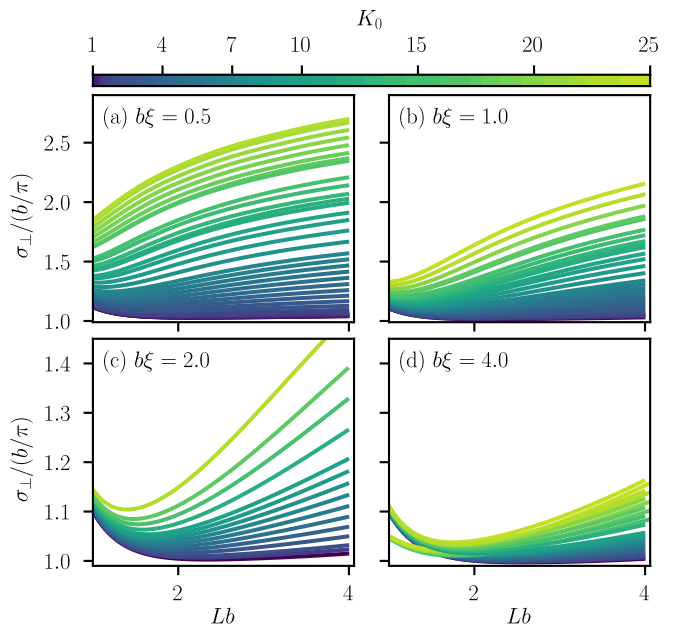


FIG. 2. Conductivity of a disordered nodal line semimetal at $\mu = 0$ as a function of length along the transport direction L . The different panels show different values of $b\xi$ and different colors denote different disorder strengths K_0 . For sufficiently large $Lb \gtrsim 2$, the conductivity increases with L and K_0 for all values of $b\xi$ for all disorder strengths we consider. All results are for $W = 20/b$ and $M_x = M_y = 19$ and averaged over up to 300 disorder realizations.

where $\langle \dots \rangle_{\text{dis}}$ denotes the disorder average. The disorder potential is characterized by the dimensionless disorder strength K_0 and the correlation length ξ . Individual disorder realizations are typically smooth and vary on the scale of ξ .

Since the disorder potential is smooth, we can ignore the path-ordering in the transfer matrix $T_{\mathbf{k}_{\perp}, \mathbf{k}'_{\perp}}(z, z')$ [Eq. (4)] when $z - z' \ll \xi$. We can thus split up the transfer matrix

$$T(L, 0) = T(z_N, z_{N-1}) \dots T(z_1, z_0) \quad (9)$$

into a product of transfer matrices for slices with $z_0 = 0$, $z_N = L$, and $z_{j+1} - z_j \ll \xi$, which we evaluate numerically [7, 42, 43]. For the numerical evaluation, we work in the limit $W \gg L$ in which σ_{\perp} depends only on L , but not on W .

To work with finite-size matrices, we introduce a momentum cutoff $|k_j| \leq k_j^{\text{max}} = 2\pi M/W$ with integer M and $j = x, y$. Unlike in graphene [7] or Weyl semimetals [12], we cannot compute the transmission for arbitrary large system widths W since the momentum cutoff needs to be larger than the nodal line radius, $2\pi M/W > b$; since M is limited by computational resources, Wb (and hence Lb for fixed W/L) is limited to a maximal value as well.

We show the ensemble-averaged conductivity σ_{\perp} divided by b/π as a function of L in Fig. 2. The color de-

notes the disorder strength K_0 and different panels show different values of $b\xi$.

We find that the conductivity increases with the strength of the disorder potential. This increase is stronger for small values of $b\xi$. These results are compatible with the behavior described in Ref. 35, where it was argued that long-range impurities lead to a weak anti-localization, i.e., an enhanced conductivity compared with the clean case [35]. Here, going beyond the perturbative regime, we find that the system remains metallic for a wide range of disorder strengths with no indication of a transition to an insulator for large K_0 . We stress that we expect this behavior to hold only for long-range disorder: For short-range (uncorrelated white noise) disorder, previous works found weak localization, i.e., a decreasing conductivity [35], and eventually a transition to an Anderson-localized regime for strong disorder [37]. At very large Lb , a similar transition to weak localization with a fixed conductivity could occur, as we explore perturbatively in Sec. III A.

The crossover from weak anti-localization for long-range disorder to weak localization for short-range disorder can be understood as a crossover from 2D diffusion to 3D diffusion [35]: For $\mu \neq 0$, the Fermi surface is effectively a torus. When the momentum-space range of the scattering potential $1/\xi < b$, backscattering is effectively limited to opposite poloidal directions, i.e., backscattering occurs within 2D planes along a fixed toroidal direction of the torus. In contrast, when $1/\xi > b$, backscattering can occur between opposite toroidal directions, leading to a 3D diffusive behavior [35]. Our results indicate that the 2D diffusion also holds for $\mu = 0$.

We verify the 2D behavior by a one-parameter scaling of the conductivity: The number of states at the Fermi level is $n \sim bW$, which independently contribute to the dimensionless conductance $g = ng_{2D}$ where g_{2D} is the 2D conductance $g_{2D} = \sigma_{2D}W/L$. 2D scaling implies that σ_{2D} follows a one-parameter scaling for large $L > 1/b$ and $L \gtrsim l_{\text{mfp}}$, where l_{mfp} is the mean free path. Since the system is at $m = 0$ in symmetry class AII, we expect $\sigma_{2D} = (1/\pi) \log(L/\ell)$ [2] to hold for large values of σ_{2D} . Then the 3D conductivity $\sigma_{\perp} = b/\pi \log(L/\ell)$ where the length ℓ depends on the disorder strength and on $b\xi$. For sufficiently large $b\xi$, the conductivity $\sigma_{\perp}/(b/\pi)$ collapses onto the same line, which we show in Fig. 3. We find a smooth scaling for $b\xi = 2$ [panel (a)] and $b\xi = 4$ [panel (b)].

A. Perturbative approach: Vertex correction

In this section, we compute the conductivity perturbatively using the self-consistent Born approximation (SCBA) to complement the transfer matrix results. While the transfer-matrix approach is well-suited to study the 2D-diffusive regime and the crossover to 3D diffusion, the perturbative calculation gives the 3D results in the limit of large system sizes, $L \gg 1/b$ and

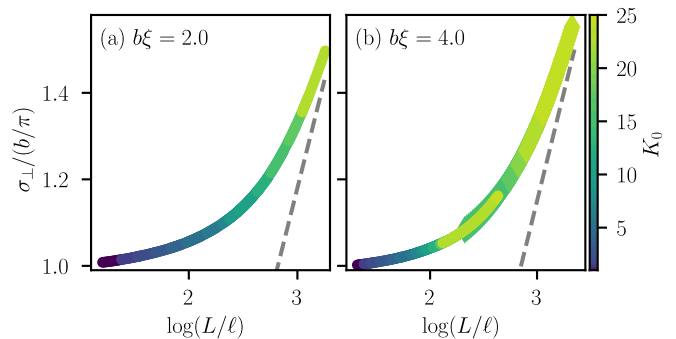


FIG. 3. Rescaled conductivity of a disordered nodal line semimetal, data from Fig. 2 for $L \gtrsim l_{\text{mfp}}$. For sufficiently large $b\xi$ [$b\xi = 2$ in panel (a) and $b\xi = 4$ in panel (b)], we can find a length ℓ such that σ_{\perp} follows the same scaling for all K_0 as a smooth function of L/ℓ . Triangles in (b) are for $W = 40/b$ ($Lb \leq 8$), discs for $W = 20/b$ ($Lb \leq 4$). Both curves collapse for sufficiently large Lb . The dashed lines denote the asymptotic $\sigma_{\perp} = b/\pi \log(L/\ell)$ scaling.

$L \gg \xi$. We follow previous approaches carried out for graphene [50] and Weyl semimetals [51], but need to resort to numerically evaluated expressions at early stages of the calculation due to the anisotropy of the model. We briefly sketch the derivation for the nodal line semimetal within the SCBA before presenting the results.

The starting point is the Hamiltonian (1), which, for $m = V(\mathbf{r}) = 0$, can, by a momentum-dependent unitary transformation $\mathcal{H}'_{\mathbf{k}} = \mathcal{U}_{\mathbf{k}} \mathcal{H}_{\mathbf{k}} \mathcal{U}_{\mathbf{k}}^{\dagger}$, be brought into a block-diagonal form

$$\mathcal{H}'_{\mathbf{k}} = \begin{pmatrix} \mathcal{H}_{-} & 0 \\ 0 & \mathcal{H}_{+} \end{pmatrix} \quad (10)$$

with $\mathcal{H}_{\pm} = (k \pm b)\sigma_y + k_z\sigma_x$ and $k = \sqrt{k_x^2 + k_y^2}$ in polar coordinates. When $b > 0$, \mathcal{H}_{+} is gapped and \mathcal{H}_{-} is gapless; note that \mathcal{H}_{-} has been previously considered as an effective Hamiltonian for a nodal line semimetal [52]. Disorder couples both blocks since the transformed potential $V'_{\mathbf{k}-\mathbf{k}'} = \mathcal{U}_{\mathbf{k}} V_{\mathbf{k}-\mathbf{k}'} \mathcal{U}_{\mathbf{k}'}^{\dagger}$ is generally off-diagonal, e.g., when $V_{\mathbf{k}-\mathbf{k}'} = u_{\mathbf{k}-\mathbf{k}'} \mathbb{1}$, we have $V_{\mathbf{k}-\mathbf{k}'} \rightarrow V'_{\mathbf{k}-\mathbf{k}'} = u_{\mathbf{k}-\mathbf{k}'} \mathcal{Q}(\phi - \phi')$ with

$$\mathcal{Q}(\phi) = \begin{pmatrix} \cos(\phi/2)\sigma_0 & -i \sin(\phi/2)\sigma_x \\ -i \sin(\phi/2)\sigma_x & \cos(\phi/2)\sigma_0 \end{pmatrix} \quad (11)$$

With the Hamiltonian (10), we can iteratively compute the disorder-averaged Green's function at zero energy in the SCBA, which for the n th iteration reads

$$G_n^s(\mathbf{k}) = \frac{1}{-\mathcal{H}'_{\mathbf{k}} - \Sigma_n^s(\mathbf{k})} \quad (12)$$

with $s = 1$ for the retarded and $s = -1$ for the advanced Green's function. In the SCBA the self-energy correction

$$\Sigma_n^s(\mathbf{k}) = \sum_{\mathbf{k}'} \langle |u_{\mathbf{k}-\mathbf{k}'}|^2 \rangle_{\text{dis}} \mathcal{Q}(\phi - \phi') G_{n-1}^s(\mathbf{k}') \mathcal{Q}(\phi' - \phi), \quad (13)$$

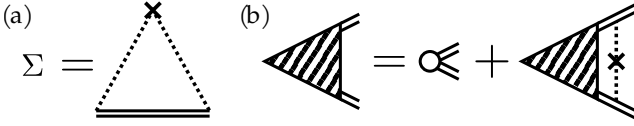


FIG. 4. (a) Diagrammatic representation of the self-energy correction in the SCBA. The double solid line represents the disorder-averaged Green's function and the dashed lines disorder scattering. (b) Diagrammatic representation of the vertex correction. The triangle represents the velocity-vertex operator and the circle the bare velocity operator (here: σ_x).

as diagrammatically represented in Fig. 4(a). Eqs. (12) and (13) give coupled, self-consistent equations, with the disorder average $\langle |u_{\mathbf{q}}|^2 \rangle_{\text{dis}}$ from (8) and the self-energy $\Sigma_0^s = -is\eta\sigma_0\tau_0$ in the initial iteration, where $\eta > 0$ is a small parameter chosen such that it does not affect the results for $n \gg 1$.

Since $G_n^s(\mathbf{k})$ depends only on the cylindrical coordinates k and k_z but not on the angle ϕ , we can perform the integration over ϕ' in Eq. (13) without prior knowledge of the Green's function itself. For scalar disorder, the Green's function and self-energy remain block-diagonal for all SCBA iterations, namely

$$\Sigma_n^s(\mathbf{k}) = \frac{K_0\xi}{2} \left(\frac{\hbar v}{2\pi} \right)^2 \int dk'_z dk k' e^{-\frac{\xi^2}{2}[(k_z - k'_z)^2 + (k^2 + k'^2)]} \times \left(I_0(\xi^2 k k') \tilde{G}_{n-1}^{s,+}(\mathbf{k}') + I_1(\xi^2 k k') \tilde{G}_{n-1}^{s,-}(\mathbf{k}') \right) \quad (14)$$

with the modified Bessel functions of the first kind $I_0(x)$ and $I_1(x)$, and the block-diagonal

$$\tilde{G}_n^{s,\pm}(\mathbf{k}) = G_n^s(\mathbf{k}) \pm \tau_x \sigma_x G_n^s(\mathbf{k}) \sigma_x \tau_x \quad (15)$$

$$= \begin{pmatrix} g_{n,\mathbf{k}}^{s,-} \pm \sigma_x g_{n,\mathbf{k}}^{s,+} \sigma_x & \\ & g_{n,\mathbf{k}}^{s,+} \pm \sigma_x g_{n,\mathbf{k}}^{s,-} \sigma_x \end{pmatrix}, \quad (16)$$

where the $g_{n,\mathbf{k}}^{s,\mp}$ are the upper and lower blocks of the Green's function

$$G_n^s(\mathbf{k}) = \begin{pmatrix} g_{n,\mathbf{k}}^{s,-} & \\ & g_{n,\mathbf{k}}^{s,+} \end{pmatrix}. \quad (17)$$

We now turn to the velocity-vertex operator, diagrammatically represented in Fig. 4(b). For transport along z , the bare velocity operator $J_0^{ss'} = (1/\hbar v) \partial_{k_z} \mathcal{H}'_{\mathbf{k}} = \sigma_x$, giving the velocity-vertex operator [50, 51]

$$J_n^{ss'}(\mathbf{k}) = \sigma_x + \sum_{\mathbf{k}'} \langle V'_{\mathbf{k}-\mathbf{k}'} G^s(\mathbf{k}') J_{n-1}^{ss'}(\mathbf{k}') G^s(\mathbf{k}') V'_{\mathbf{k}'-\mathbf{k}} \rangle_{\text{dis}} \quad (18)$$

where $G^s(\mathbf{k}) = \lim_{n \rightarrow \infty} G_n^s(\mathbf{k})$ is the disorder-averaged Green's function in the SCBA approximation. Here we again perform the integration over ϕ' analytically before numerically integrating over k' and k'_z .

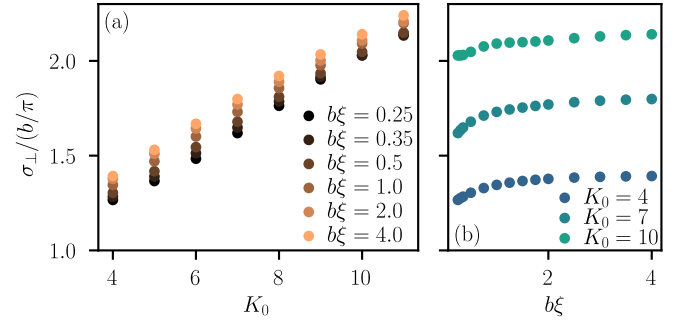


FIG. 5. Out-of-plane conductivity σ_{\perp} computed via the vertex correction, Eq. (19). (a) Conductivity as a function of disorder strength K_0 with colors denoting $b\xi$. (b) Conductivity as a function of $b\xi$ with colors denoting K_0 .

Finally, the conductivity divided by e^2/h [50, 51]

$$\sigma_{\perp} = -\frac{(\hbar v)^2}{2} \sum_{s,s'} ss' \int \frac{d^3\mathbf{k}}{(2\pi)^3} \text{tr}[\sigma_x G^s(\mathbf{k}) J^{ss'}(\mathbf{k}) G^{s'}(\mathbf{k})] \quad (19)$$

where $J^{ss'}(\mathbf{k}) = \lim_{n \rightarrow \infty} J_n^{ss'}(\mathbf{k})$ is the disorder-averaged velocity-vertex operator in the SCBA approximation. We show σ_{\perp} in Fig. (5).

We find that the conductivity increases with K_0 [Fig. (5)(a)], which supports the findings we obtained with the transfer matrix method presented in Sec. III. Furthermore, σ_{\perp}/b increases with $b\xi$ and for $b\xi \gtrsim 1$, σ_{\perp}/b approaches a $b\xi$ -independent constant, which is consistent with $\sigma_{\perp}/b \propto \sqrt{(\Gamma/b)^2 + 1}$ found previously for a momentum- and energy-independent level-broadening Γ [38]. Since we find that σ_{\perp}/b is $b\xi$ -independent for $b\xi \gtrsim 1$, our results indicate that Γ/b depends only on K_0 in this regime.

Since the conductivity we obtain via the transfer matrix method does not saturate for the system sizes we can achieve numerically, we cannot compare the perturbative SCBA 3D results with the (exact for sufficiently large M) transfer matrix results.

B. Symmetry-breaking vector potential

In this section we demonstrate that the system remains metallic in the presence of disorder that breaks the symmetry protecting the nodal line. Adding a term $u_0\Gamma_5$ to the Hamiltonian (1) opens a gap: $u_0\Gamma_5$ breaks both the effective time-reversal symmetry, and inversion symmetry, which protects the nodal line. Unlike other inversion-symmetry-breaking terms that give rise to a Weyl semimetal phase [17], $u_0\Gamma_5$ opens a gap everywhere in the spectrum and the system becomes insulating.

To demonstrate the stability of the metallic phase towards symmetry-breaking disorder, we now consider a disorder potential of the form $V(\mathbf{r}) = u(\mathbf{r})\Gamma_5$. In Fig. 6(a), we show numerical results for $u_0 \equiv \langle u(\mathbf{r}) \rangle_{\text{dis}} = 0$ and correlated disorder with strength K_0 and range ξ

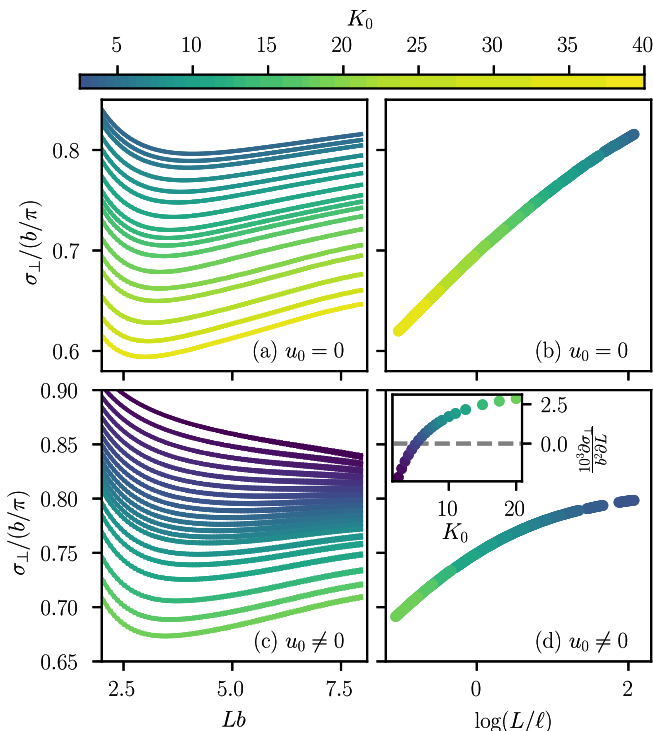


FIG. 6. Conductivity σ_{\perp} for vector disorder of the form $V(\mathbf{r}) = u(\mathbf{r})\Gamma_5$. (a) Conductivity for $u_0 = 0$, $b\xi = 2$ and various disorder strengths up to $K = 40$ as a function of Lb and (b) as a function of $\log(L/\ell)$ for $L \gtrsim l_{\text{mfp}}$. (c) Conductivity for $u_0 = 0.1\hbar v/\xi$, $b\xi = 2$ and various disorder strengths as a function of Lb and (d) for as a function of $\log(L/\ell)$ for $K_0 \geq 6$. The inset in (d) shows the slope $\partial\sigma_{\perp}/\partial L$ of linear fit for $7 \leq Lb \leq 8$.

[Eq. (8)] for a wide range of disorder strengths K_0 and fixed $\xi b = 2$. We find that, although the conductivity itself decreases with K_0 , the system remains metallic for all K_0 we consider. We cannot exclude a transition to an insulating phase for larger values of $K_0 > 40$.

The symmetry-breaking disorder $\propto \Gamma_5$ may also drive a transition from an insulating to a metallic regime: In Fig. 6(c), we show numerical results for $u_0 \neq 0$ and $b\xi = 2$. In the absence of disorder, i.e., for $\langle u(\mathbf{r})u(\mathbf{r}') \rangle_c = \langle u(\mathbf{r})u(\mathbf{r}') \rangle_{\text{dis}} - u_0^2 = 0$, the system is gapped and therefore insulating. For weak disorder, the conductivity is initially nonzero, but decreases with system size. For strong disorder $K_0 > K_c$ with $K_c = 5.25 \pm 0.5$, the conductivity increases with system size and follows a one-parameter scaling, cf. Fig. 6(d). Different from the case of scalar disorder, the conductivity does not grow indefinitely but flows towards a threshold value $\sigma_{\perp}/(b/\pi) = 0.8 \pm 0.05$. (The data collapse for a rescaled L is not possible for $K_0 < K_c$.) As we show in the inset in Fig. 6(d), the conductivity σ_{\perp} decreases with L below the threshold and increases with L above the threshold, indicating a metal-insulator transition at K_c . Since the conductivity for $K_0 < K_c$ is always $\sigma_{\perp}/(b/\pi) \gtrsim 0.8$, an alternative scenario is a flow towards the same threshold value

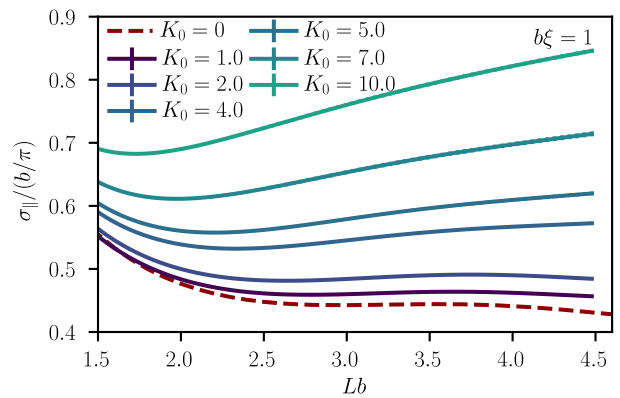


FIG. 7. Conductivity σ_{\parallel} of a disordered nodal line semimetal as a function of the length along the transport direction L with \mathbf{b} orthogonal to the transport direction, i.e., transport in the plane of the nodal line. Colors denote different disorder strengths K_0 . Apart from oscillations pronounced for small K_0 , the conductivity increases with L and K_0 for all disorder strengths we consider. Results are averaged over up to 200 disorder realizations.

for $K_0 < K_c$. A more detailed analysis is necessary to determine whether the system always tends towards an insulator below threshold.

We note that a similar behavior has been observed for 2D class-D superconductors [53] and weak topological insulator surface states [54] with a random mass term, which at the transition between two distinct insulators (corresponding to $\langle u(\mathbf{r}) \rangle_{\text{dis}} = 0$ here) remain metallic when disorder is added [55], and which away from the transition, i.e., starting from an insulating phase, are driven to a metallic phase. Note that details of the phase diagrams in classes D [53] and AII [54] differ around the transition line. We leave the investigation of these details of the phase diagrams in 3D nodal line semimetals for future works.

IV. IN-PLANE TRANSPORT

We now turn to transport in the plane of the nodal line in the presence of disorder. In Fig. 7, we show the conductivity σ_{\parallel} obtained using the transfer matrix approach as a function of L for various values of K_0 and fixed $b\xi = 1$. We also included the $K_0 = 0$ results [cf. Fig. 1(b)] to show the clean-case oscillations as a function of Lb .

For weak disorder, the oscillations in Lb remains stable until they become indiscernible from the increasing trend when $K_0 \sim 7$. Analog to transport out of the plane of the nodal line, we see that the conductivity generally increases with K_0 . We expect that rescaling the conductivity analog to the data shown in Fig. 3 is possible for sufficiently large system sizes when the oscillations do not play a role, although we did not attempt such a rescaling here.

V. CONCLUSION AND OUTLOOK

In this work, we used a transfer matrix approach to show that the conductivity of a nodal line semimetal increases with disorder and that the system remains metallic for all disorder strengths investigated. This holds for both transport directions, i.e., orthogonal to, and in the plane of the nodal line. The metallic behavior is also sustained by the results obtained using the Kubo formula in the self-consistent Born approximation. The system remains metallic even in the presence of vector disorder that breaks inversion symmetry, which crucially protects the nodal line; such correlated vector disorder can also drive a transition from an insulator to a metal.

We found oscillations in the conductivity for transport in the plane of the nodal line, which persist for weak disorder. These oscillations decay with system size, such that, in the clean case, the conductivity goes to a constant for large systems. However, the transfer matrix result does not match the Kubo formula result.

In real materials, various effects might play a role that we did not consider in this work: First, a nonzero chemical potential changes the Fermi surface to a torus [28, 52]. While the crossover from a 2D to a 3D transport regime was originally predicted for a torus-shaped Fermi surface [35], the conductivity growth with disorder is likely to be affected by moving the chemical potential away from the nodal line. Furthermore, a BCS-like disorder-driven transition has been predicted for $\mu \neq 0$ [14, 56] that implies a different scaling of density of states and conductivity above and below a critical disorder strength. (At $\mu = 0$, the critical disorder strength is zero [14].) Second, we consider a simplified model with only terms linear in momentum terms contributing to the Hamiltonian. Terms that are higher order in momentum will introduce more length scales that could provide upper cutoffs for the absence of localization we observe here. Third, we have neglected surface states throughout this work, which may alter transport properties [57]. Finally, due to the momentum cutoff we used in the numerical simulations, the results are not valid for small values of Lb .

In addition to this, our results are valid only in the non-interacting regime. Interaction effects may nontrivially interplay with disorder in nodal line semimetals [58, 59].

This interplay can, unlike in parabolic systems [60], affect transport [59].

Evading localization is generally linked to topological terms [5, 6, 61]. The metal we find for all disorder strengths hints that a topological term might also play a role in nodal line semimetals. Previous works had found a 3D analog [62, 63] of the θ term in graphene [6]. This term might influence transport away from the clean case and could be linked to the absence of localization we found.

Possible extensions of our work could explore $\mu \neq 0$ and the consequences of the BCS-like transition for transport [14, 56]. Furthermore, it would be interesting to explore the phase diagram of the potential $V(\mathbf{r}) = (u_0 + u(\mathbf{r}))\Gamma_5$ that opens a gap everywhere in the spectrum.

ACKNOWLEDGMENTS

The authors are grateful to Jens H. Bardarson for insightful discussions throughout the project and careful reading of the manuscript. JB thanks Jun-Won Rhim for helpful discussions, especially in the early stages of this work. JB is supported by a Leverhulme Early Career Fellowship, and the Newton Trust of the University of Cambridge.

Our simulations used resources at the Cambridge Service for Data Driven Discovery operated by the University of Cambridge Research Computing Service (www.csd3.cam.ac.uk), provided by Dell EMC and Intel using EPSRC Tier-2 funding via grant EP/T022159/1, and STFC DiRAC funding (www.dirac.ac.uk).

Appendix A: Nonzero mass term

The focus in the main text is on $m = 0$, a fine-tuned point in the phase diagram where the system is effectively time-reversal symmetric. Here we discuss out-of-plane transport for $m \neq 0$, both for clean systems and disordered system with scalar disorder $V(\mathbf{r}) = u(\mathbf{r})\mathbf{1}$. In the clean case, i.e., for $u(\mathbf{r}) = 0$ and for transport parallel to $\mathbf{b} = b\mathbf{e}_z$, we solve the transfer matrix [Eq. (4) in the main text], giving the trace

$$\mathrm{tr}[t^\dagger t] = \frac{1}{\cosh^2 [L(b + \sqrt{k^2 + \tilde{m}^2})]} + \frac{1}{\cosh^2 [L(b - \sqrt{k^2 + \tilde{m}^2})]} \quad (\text{A1})$$

where $\tilde{m} = m/(\hbar v)$ for a compact notation and $0 \leq \tilde{m} < b$ for a gapless system. In the limit $W \gg L$, the dimensionless conductance is accordingly

$$g_\perp = \frac{W^2}{2\pi} \int dk k \mathrm{tr}[t^\dagger t] = \frac{W^2}{L} \frac{b}{\pi} \left(\frac{\log [2(\cosh(2L\tilde{m}) + \cosh(2Lb))]}{2Lb} - \frac{\tilde{m} \sinh(2L\tilde{m})}{2b \cosh(L(b - \tilde{m})) \cosh(L(b + \tilde{m}))} \right) \quad (\text{A2})$$

and the conductivity $\sigma_\perp \xrightarrow{Lb \gg 1} b/\pi$, the same value we

obtained in the main text for $m = 0$. We show the σ_\perp as

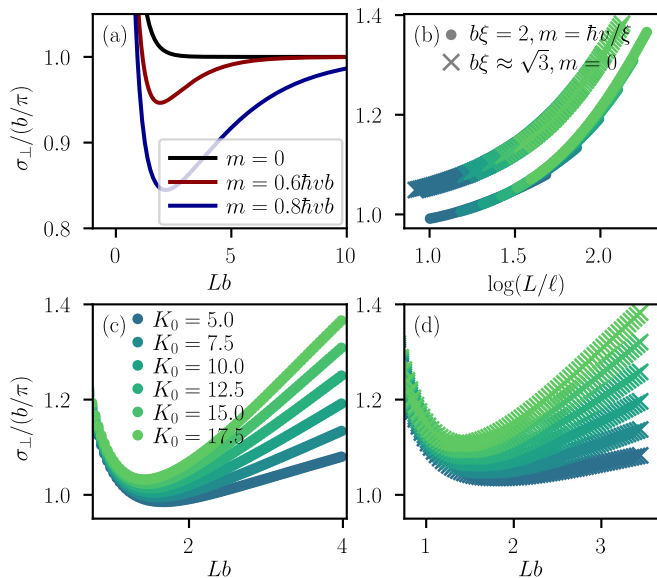


FIG. 8. (a) Out-of-plane conductivity σ_{\perp} in the clean case for different values of m , cf. Eq. (A2). (b) σ_{\perp} as a function of the rescaled system length L/ℓ for different values of K_0 , where crosses denote $b\xi = 2$ and $m = \hbar v/\xi$ (with $b_{\text{eff}}\xi = \sqrt{3}$), and dots denote $b\xi = 1.73 \approx \sqrt{3}$ and $m = 0$. The data does not perfectly collapse when $m \neq 0$. (c) Raw conductivity data for $m \neq 0$ and (d) for $m = 0$ with the same nodal line radius.

a function of Lb for different values of m in Fig. 8(a).

The term $m \neq 0$ breaks the emergent time-reversal symmetry discussed in the main text. To confirm that the behavior we find for disordered nodal line semimetals does not rely on the presence of this emergent time-reversal symmetry, we here consider disordered systems with $m \neq 0$. In Fig. 8(b), we show the rescaled conductivity as a function of $\log(L/\ell)$ for different disorder strength and for $b\xi = 2$, $m/(\hbar v/\xi) = 1$ and $b\xi = 1.73 \approx \sqrt{3}$, $m = 0$. The radius of the nodal line in clean systems is in both cases $b_{\text{eff}} = \sqrt{b^2 - (m/(\hbar v))^2} \approx \sqrt{3}/\xi$.

Importantly, even when $m \neq 0$, the conductivity increases with both L and K_0 . However, the data does not collapse onto the same line for $m \neq 0$, indicating that the 2D scaling does hold only approximately here. For completeness, we show the raw data in Fig. 8(c) and (d).

-
- [1] E. Abrahams, P. W. Anderson, D. C. Licciardello, and T. V. Ramakrishnan, Scaling Theory of Localization: Absence of Quantum Diffusion in Two Dimensions, *Physical Review Letters* **42**, 673 (1979).
 - [2] F. Evers and A. D. Mirlin, Anderson transitions, *Reviews of Modern Physics* **80**, 1355 (2008).
 - [3] S. Hikami, Three-loop β -functions of non-linear σ models on symmetric spaces, *Physics Letters B* **98**, 208 (1981).
 - [4] R. Gade and F. Wegner, The $n = 0$ replica limit of $U(n)$ and models, *Nuclear Physics B* **360**, 213 (1991).
 - [5] A. Pruisken, On localization in the theory of the quantized hall effect: A two-dimensional realization of the θ -vacuum, *Nuclear Physics B* **235**, 277 (1984).
 - [6] P. M. Ostrovsy, I. V. Gornyi, and A. D. Mirlin, Quantum Criticality and Minimal Conductivity in Graphene with Long-Range Disorder, *Physical Review Letters* **98**, 256801 (2007).
 - [7] J. H. Bardarson, J. Tworzydło, P. W. Brouwer, and C. W. J. Beenakker, One-Parameter Scaling at the Dirac Point in Graphene, *Physical Review Letters* **99**, 106801 (2007).
 - [8] K. Nomura, M. Koshino, and S. Ryu, Topological Delocalization of Two-Dimensional Massless Dirac Fermions, *Physical Review Letters* **99**, 146806 (2007).
 - [9] R. Nandkishore, D. A. Huse, and S. L. Sondhi, Rare region effects dominate weakly disordered three-dimensional Dirac points, *Physical Review B* **89**, 245110 (2014).
 - [10] J. Pixley and J. H. Wilson, Rare regions and avoided quantum criticality in disordered Weyl semimetals and superconductors, *Annals of Physics* **435**, 168455 (2021).
 - [11] P. Goswami and S. Chakravarty, Quantum Criticality between Topological and Band Insulators in 3 + 1 Dimensions, *Physical Review Letters* **107**, 196803 (2011).
 - [12] B. Sbierski, G. Pohl, E. J. Bergholtz, and P. W. Brouwer, Quantum Transport of Disordered Weyl Semimetals at the Nodal Point, *Physical Review Letters* **113**, 026602 (2014).
 - [13] S. V. Syzranov and L. Radzihovsky, High-Dimensional Disorder-Driven Phenomena in Weyl Semimetals, Semiconductors and Related Systems, *Ann. Rev. Cond. Mat. Phys* **9**, 35 (2017).
 - [14] S. Zhu and S. Syzranov, BCS-like disorder-driven instabilities and ultraviolet effects in nodal-line semimetals, *Annals of Physics* **459**, 169501 (2023).
 - [15] T. T. Heikkilä and G. E. Volovik, Dimensional crossover in topological matter: Evolution of the multiple Dirac point in the layered system to the flat band on the surface, *JETP Letters* **93**, 59 (2011).
 - [16] B. Béri, Topologically stable gapless phases of time-reversal-invariant superconductors, *Physical Review B* **81**, 134515 (2010).
 - [17] A. A. Burkov, M. D. Hook, and L. Balents, Topological nodal semimetals, *Phys. Rev. B* **84**, 235126 (2011).
 - [18] C.-K. Chiu and A. P. Schnyder, Classification of reflection-symmetry-protected topological semimetals and nodal superconductors, *Physical Review B* **90**, 205136 (2014).
 - [19] Z. Yang, C.-K. Chiu, C. Fang, and J. Hu, Jones Polynomial and Knot Transitions in Hermitian and non-

- Hermitian Topological Semimetals, *Physical Review Letters* **124**, 186402 (2020).
- [20] M. Phillips and V. Aji, Tunable line node semimetals, *Physical Review B* **90**, 115111 (2014).
- [21] C. Fang, Y. Chen, H.-Y. Kee, and L. Fu, Topological nodal line semimetals with and without spin-orbital coupling, *Physical Review B* **92**, 081201 (2015).
- [22] Y. H. Chan, C. K. Chiu, M. Y. Chou, and A. P. Schnyder, Ca₃P₂ and other topological semimetals with line nodes and drumhead surface states, *Phys. Rev. B* **93**, 205132 (2016).
- [23] T. Bzdušek and M. Sigrist, Robust doubly charged nodal lines and nodal surfaces in centrosymmetric systems, *Physical Review B* **96**, 155105 (2017).
- [24] J. Wang, Antiferromagnetic topological nodal line semimetals, *Physical Review B* **96**, 081107 (2017).
- [25] J. Behrends, J.-W. Rhim, S. Liu, A. G. Grushin, and J. H. Bardarson, Nodal-line semimetals from Weyl superlattices, *Phys. Rev. B* **96**, 245101 (2017).
- [26] G. Bian, T.-R. Chang, R. Sankar, S.-Y. Xu, H. Zheng, T. Neupert, C.-K. Chiu, S.-M. Huang, G. Chang, I. Belopolski, D. S. Sanchez, M. Neupane, N. Alidoust, C. Liu, B. Wang, C.-C. Lee, H.-T. Jeng, C. Zhang, Z. Yuan, S. Jia, A. Bansil, F. Chou, H. Lin, and M. Z. Hasan, Topological nodal-line fermions in spin-orbit metal Pb-TaSe₂, *Nature Communications* **7**, 10556 (2016).
- [27] L. M. Schoop, M. N. Ali, C. Straßer, A. Topp, A. Varykhalov, D. Marchenko, V. Duppel, S. S. P. Parkin, B. V. Lotsch, and C. R. Ast, Dirac cone protected by non-symmorphic symmetry and three-dimensional Dirac line node in ZrSiS, *Nature Communications* **7**, 11696 (2016).
- [28] D. Takane, K. Nakayama, S. Souma, T. Wada, Y. Okamoto, K. Takenaka, Y. Yamakawa, A. Yamakage, T. Mitsuhashi, K. Horiba, H. Kumigashira, T. Takahashi, and T. Sato, Observation of Dirac-like energy band and ring-torus Fermi surface associated with the nodal line in topological insulator CaAgAs, *npj Quantum Materials* **3**, 1 (2018).
- [29] T.-R. Chang, I. Pletikovic, T. Kong, G. Bian, A. Huang, J. Denlinger, S. K. Kushwaha, B. Sinkovic, H.-T. Jeng, T. Valla, W. Xie, and R. J. Cava, Realization of a Type-II Nodal-Line Semimetal in Mg₃Bi₂, *Advanced Science* **6**, 1800897 (2019).
- [30] B.-B. Fu, C.-J. Yi, T.-T. Zhang, M. Caputo, J.-Z. Ma, X. Gao, B. Q. Lv, L.-Y. Kong, Y.-B. Huang, P. Richard, M. Shi, V. N. Strocov, C. Fang, H.-M. Weng, Y.-G. Shi, T. Qian, and H. Ding, Dirac nodal surfaces and nodal lines in ZrSiS, *Science Advances* **5**, 1 (2019).
- [31] B. Q. Lv, T. Qian, and H. Ding, Experimental perspective on three-dimensional topological semimetals, *Reviews of Modern Physics* **93**, 025002 (2021).
- [32] W. Deng, J. Lu, F. Li, X. Huang, M. Yan, J. Ma, and Z. Liu, Nodal rings and drumhead surface states in phononic crystals, *Nature Communications* **10**, 1769 (2019).
- [33] B. Song, C. He, S. Niu, L. Zhang, Z. Ren, X.-J. Liu, and G.-B. Jo, Observation of nodal-line semimetal with ultracold fermions in an optical lattice, *Nature Physics* **15**, 911 (2019).
- [34] S. V. Syzranov and B. Skinner, Electron transport in nodal-line semimetals, *Physical Review B* **96**, 161105 (2017).
- [35] W. Chen, H.-Z. Lu, and O. Zilberberg, Weak Localization and Antilocalization in Nodal-Line Semimetals: Dimensionality and Topological Effects, *Physical Review Letters* **122**, 196603 (2019).
- [36] M.-X. Yang, W. Luo, and W. Chen, Quantum transport in topological nodal-line semimetals, *Advances in Physics: X* **7**, 2065216 (2022).
- [37] M. Gonçalves, P. Ribeiro, E. V. Castro, and M. A. Araújo, Disorder-Driven Multifractality Transition in Weyl Nodal Loops, *Physical Review Letters* **124**, 136405 (2020).
- [38] S. P. Mukherjee and J. P. Carbotte, Transport and optics at the node in a nodal loop semimetal, *Physical Review B* **95**, 214203 (2017).
- [39] L. An, X. Zhu, W. Gao, M. Wu, W. Ning, and M. Tian, Chiral anomaly and nontrivial Berry phase in the topological nodal-line semimetal SrAs₃, *Physical Review B* **99**, 045143 (2019).
- [40] A. Laha, S. Malick, R. Singha, P. Mandal, P. Rambabu, V. Kanchana, and Z. Hossain, Magnetotransport properties of the correlated topological nodal-line semimetal YbCdGe, *Physical Review B* **99**, 241102 (2019).
- [41] T. Zhou, M. Tong, X. Xie, Y. Yu, X. Zhu, Z.-Y. Wang, and T. Jiang, Quantum Transport Signatures of a Close Candidate for a Type II Nodal-Line Semimetal, *The Journal of Physical Chemistry Letters* **11**, 6475 (2020).
- [42] V. V. Cheianov and V. I. Fal'ko, Selective transmission of Dirac electrons and ballistic magnetoresistance of *n-p* junctions in graphene, *Physical Review B* **74**, 041403 (2006).
- [43] M. Titov, Impurity-assisted tunneling in graphene, *Europhysics Letters (EPL)* **79**, 17004 (2007).
- [44] P. A. Mello, P. Pereyra, and N. Kumar, Macroscopic approach to multichannel disordered conductors, *Annals of Physics* **181**, 290 (1988).
- [45] H. Tamura and T. Ando, Conductance fluctuations in quantum wires, *Physical Review B* **44**, 1792 (1991).
- [46] C. W. J. Beenakker, Random-matrix theory of quantum transport, *Reviews of Modern Physics* **69**, 731 (1997).
- [47] We use the following convention for gamma matrices: $\Gamma_1 = \tau_1\sigma_1$, $\Gamma_2 = \tau_1\sigma_2$, $\Gamma_3 = \tau_3$, $\Gamma_4 = \tau_1\sigma_3$ and $\Gamma_5 = -\tau_2$.
- [48] J. Behrends, *Transport and Quantum Anomalies in Topological Semimetals*, Ph.D. thesis, Technische Universität Dresden (2018).
- [49] We thank Jun-Won Rhim for this observation.
- [50] M. Noro, M. Koshino, and T. Ando, Theory of Transport in Graphene with Long-Range Scatterers, *Journal of the Physical Society of Japan* **79**, 094713 (2010).
- [51] Y. Ominato and M. Koshino, Quantum transport in a three-dimensional Weyl electron system, *Phys. Rev. B* **89**, 054202 (2014).
- [52] J.-W. Rhim and Y. B. Kim, Anisotropic density fluctuations, plasmons, and Friedel oscillations in nodal line semimetal, *New Journal of Physics* **18**, 043010 (2016).
- [53] M. V. Medvedyeva, J. Tworzydło, and C. W. J. Beenakker, Effective mass and tricritical point for lattice fermions localized by a random mass, *Physical Review B* **81**, 214203 (2010).
- [54] R. S. K. Mong, J. H. Bardarson, and J. E. Moore, Quantum transport and two-parameter scaling at the surface of a weak topological insulator, *Physical Review Letters* **108**, 076804 (2012).
- [55] In class D, the system only becomes metallic for white-noise disorder [53, 64].
- [56] S. Sun and S. Syzranov, Interactions-disorder duality and

- critical phenomena in nodal semimetals, dilute gases, and other systems, *Physical Review B* **108**, 195132 (2023).
- [57] J.-J. Fu, S.-T. Guan, J. Xie, and J. An, Quantum Transport on the Surfaces of Topological Nodal-line Semimetals, [arXiv:2309.03699](https://arxiv.org/abs/2309.03699).
- [58] Y. Wang and R. M. Nandkishore, Interplay between short-range correlated disorder and Coulomb interaction in nodal-line semimetals, *Physical Review B* **96**, 115130 (2017).
- [59] D. Muñoz-Segovia and A. Cortijo, Many-body effects in nodal-line semimetals: Correction to the optical conductivity, *Physical Review B* **101**, 205102 (2020).
- [60] W. Kohn, Cyclotron Resonance and de Haas-van Alphen Oscillations of an Interacting Electron Gas, *Physical Review* **123**, 1242 (1961).
- [61] D. E. Khmel'nitskii, Quantization of Hall conductivity, *Pis'ma Zh. Exp. Teor. Fiz.* **38**, 454 (1983), [*JETP Lett.* **38**, 552–556 (1983)].
- [62] A. A. Burkov, Quantum anomalies in nodal line semimetals, *Phys. Rev. B* **97**, 165104 (2018).
- [63] W. B. Rui, Y. X. Zhao, and A. P. Schnyder, Topological transport in Dirac nodal-line semimetals, *Physical Review B* **97**, 161113 (2018).
- [64] J. H. Bardarson, M. V. Medvedyeva, J. Tworzydło, A. R. Akhmerov, and C. W. J. Beenakker, Absence of a metallic phase in charge-neutral graphene with a random gap, *Physical Review B* **81**, 121414 (2010).